Journal of Constructional Steel Research 227 (2025) 109370

Contents lists available at ScienceDirect

Journal of Constructional Steel Research

journal homepage: www.elsevier.com/locate/jcsr

Numerical investigation of cyclic behaviour in H-shaped stainless-steel beam-columns

Asal Pournaghshband [a,*], Roham Maher [b]

[a] Centre for Engineering Research, School of Physics, Engineering and Computer Science, University of Hertfordshire, Hatfield AL10 9AB, UK
[b] Department of Mechanical Engineering, South Tehran Branch, Islamic Azad University, Tehran, Iran

ARTICLE INFO

Keywords:
Beam-column
Cyclic performance
Numerical modelling
Parametric analysis
Stainless steel
Taguchi method

ABSTRACT

This study conducts a numerical investigation into the cyclic performance of H-shaped stainless steel beam-columns under seismic loading. Numerical models were developed and validated using experimental data from H-shaped carbon steel beam-columns subjected to cyclic bending. These models showed high predictive accuracy, with a 7.5 % margin when comparing end moments and rotations. Through the finite element approach and Taguchi method, key parameters were analysed including column length, stiffener spacing, material classification, load ratio, stiffener thickness, and number of local buckling modes. The results highlight austenitic stainless steel's exceptional deformation capacity, with enhanced elongation at fracture and superior post-yield strength compared to carbon steel. With a ductility ratio of 19.09 under a 0.4 load ratio, it surpasses ferritic and duplex stainless steels. This demonstrates superior seismic energy absorption and enhanced energy dissipation through broader hysteresis loops. Duplex stainless steel, with 30.5 % higher yield stress than austenitic grade, exhibited narrower hysteresis loops and earlier local buckling, balancing high cyclic strength with moderate ductility. This makes it ideal for stiffness-critical applications under intense cyclic demands. Ferritic stainless steel, though stronger than carbon steel, showed 50 % lower elongation than austenitic steel, with higher brittleness and inferior energy dissipation compared to duplex steel. The study underscores the role of axial load ratios in governing failure modes and deformations. These findings are pivotal for advancing design codes and enhancing structural resilience in earthquake-prone regions. They emphasize the inclusion of stainless steel in seismic design standards, addressing current limitations due to insufficient research on its cyclic behaviour.

1. Introduction

H-shaped steel structural beam-column elements are widely recognized for their versatility in industrial buildings, attributed to their high strength-to-weight ratio and excellent bending resistance [1,2]. H-shaped steel cross sections are classified into four types according to Eurocode 3, based on their local buckling resistance, which determines their strength and rotational capacity [3]. Classes 1 and 2 reach plastic moment resistance, while class 3 (semi-slender) buckles before plastic capacity, and class 4 (slender) before yield load. The behaviour of class 1 and 2 sections under monotonic loading, including weak-axis buckling and axial compression, has drawn research attention [4–6]. Steel's monotonic behaviour is significantly affected by cyclic loading, which reduces ductility due to early necking and fracture caused by cyclic loops and amplitudes [7]. The impact of local buckling due to width-thickness ratios on the plastic deformation, strength, and ductility of H-shaped steel beam-columns under cyclic loading has been studied [8,9]. Tests on non-compact and slender sections under cyclic load showed that non-compact sections provide ductility beyond the elastic limit, with simplified equations proposed to accurately predict the ultimate resistance of both sections for seismic design [10].

Recently, the criterion for allowable maximum inelastic displacements, based on strength-ductility relations, has been used in modern seismic design [11]. Design strategies to improve ductility for earthquake resistance identified local buckling as the main failure mode in high-performance steel H-section beam-columns [12]. Key factors affecting cyclic behaviour included width-to-thickness and axial load ratios, with smaller width-to-thickness ratios improving ductility and producing fuller cyclic curves. Given the limitations of carbon steel in seismic applications, particularly in terms of reduced ductility under

* Corresponding author.
E-mail address: a.pournaghshband@herts.ac.uk (A. Pournaghshband).

https://doi.org/10.1016/j.jcsr.2025.109370
Received 10 October 2024; Received in revised form 8 January 2025; Accepted 25 January 2025
Available online 30 January 2025

cyclic loads, stainless steel offers a compelling alternative. Stainless steel structural products, a sustainable alternative to carbon steel, offer benefits like fire and corrosion resistance, high strength, and improved ductility. These advantages are particularly notable in austenitic grades, which are well-suited for seismic zones [13]. Austenitic stainless steel tubular elements showed 88 % greater elongation at fracture and 35 % higher post-yield strength compared to carbon steel in cyclic tests [14]. Unlike carbon steel, stainless steel exhibits a nonlinear stress-strain relationship due to strain hardening [15]. The load capacity and deformation of austenitic stainless steel depend on cyclic loading protocols, influenced by unsaturated cyclic hardening properties [16–19]. Austenitic stainless steel maintained excellent seismic performance under the specified low cycle loading protocol [20]. Austenitic specimens with the highest strength became brittle after yielding due to austenite-to-martensite transformation, reducing ductility and energy absorption, contrary to expectations [21]. The study comparing austenitic and lean duplex stainless steel hollow sections under cyclic loading found that, despite a 30.5 % higher yield stress, duplex stainless steel experienced local buckling earlier during seismic loading [21]. Austenitic stainless steels EN 1.4301 and EN 1.4401 exhibit similar cyclic stress responses with initial hardening followed by softening. In contrast, duplex stainless steel EN 1.4462 has a higher stress amplitude, high yield strength, and effective energy dissipation, with cyclic hardening followed by prolonged softening [22,23]. An experimental study found that lean duplex stainless steel EN 1.4162 has higher maximum cyclic strength and narrower hysteresis loops than austenitic EN 1.4301 at ±2.0 % strain, but EN 1.4301 exhibits greater cyclic hardening [24]. A numerical study found that the strength and rotational capacity of stainless steel Rectangular Hollow Section (RHS) beams under cyclic loading depend on cross-section slenderness and strain hardening, with austenitic beams having slightly higher rotation capacities than ferritic and duplex beams [25]. A study found that austenitic stainless steel RHS members achieved much higher ultimate rotation under cyclic minor axis bending compared to carbon steel [26]. Moghaddam et al. [27] conducted a numerical analysis on built-up box columns under cyclic loading, revealing plastic rotation depends on the width-to-thickness ratio. Ning et al. [28,29] evaluated the hysteretic performance of stainless-steel box and H-shaped columns, showing EN 1993-1-4 offers a conservative approach for class 3 and 4 cross-sections. Stainless steel design codes conservatively predicted compressive resistance with variation, while the Continuous Strength Method (CSM) was more consistent, leading to a proposed ductility-oriented design approach [30]. Despite extensive research, limited seismic evaluation of stainless-steel members results in low confidence in their use in seismic regions, particularly for bracing members [30]. The upcoming European earthquake-resistant code, prEN 1998-1-2 [31], excludes stainless steel due to insufficient research, despite its distinct hysteretic behaviour [14,18]. This underscores the need for further study on stainless steel grades under cyclic loading to identify key factors influencing their response.

This paper investigates the cyclic behaviour of H-shaped stainless-steel columns using extensive numerical modelling to examine key factors influencing their performance. Additionally, it compares different materials, focusing on their ductility and energy dissipation characteristics. Section 2 describes the development of the numerical models and their validation against existing experimental results. Section 3 summarises numerical parametric studies using the Taguchi method and Finite Element Method (FEM) to examine the effects of key parameters, such as column length, stiffener spacing, material classification, load ratio, stiffener thickness, and local buckling modes. The research aims to optimise ductility and energy dissipation, crucial factors for seismic design. Section 4 presents a discussion of the numerical results, including a comparison of various stainless-steel grades and carbon steel.

2. Numerical model development and validation

Numerical analyses were conducted utilising the commercial finite element (FE) software ANSYS [32]. The methodology for constructing FE models of H-shaped columns was outlined in this section. To confirm the accuracy of the developed FE models, they were tested on five specimens from an earlier study. Following the validation process, parametric analyses were carried out using the established FE models.

2.1. Literature-based test plan

The numerical models developed were validated using experimental results from the literature on H-shaped carbon steel beam-column specimens subjected to constant vertical (N) and cyclic horizontal (V) loading, as depicted in Fig. 1. These experiments, conducted at Tongji University's research laboratory, involved H-shaped steel specimens with varying flange width-thickness and axial force ratios [9,33]. The study aimed to examine how section classification and loading influence weak-axis cyclic bending behaviour. The specimens, configured as cantilever beam-columns with a nominal length (L) of 1500 mm, had free rotation at the top to transfer only shear and axial forces, while the base was fixed to a reaction frame.

The specimens were fabricated from low alloy structural steel plates with thicknesses of 4 mm and 6 mm. The investigation delved into the influence of axial force ratios $n = N/(A.f_y)$ by analysing two distinct levels of 0.2 and 0.4. Here, N signifies the axial force, f_y stands for the yield stress, and A denotes the cross-sectional area of the specimens. Initially, the specimen was subjected to an axial load, which was maintained at a constant level for the duration of the test. Following this, a cyclic horizontal load was introduced, gradually amplifying lateral displacement amplitudes until reaching 10 times the nominal yield displacement ($10\Delta y$). The nominal yield displacement, denoted by Δy, was uniformly set at approximately 10 mm for all specimens, determined through calculations based on monotonic loading characteristics. This ensured consistency across the specimens in terms of the applied load conditions. The geometric properties of the specimens are detailed in Table 1, utilising measured attributes. In this context, h and b correspond to the total height and total width of the H-shaped cross-section, while t_w and t_f denote the web thickness and flange thickness, respectively. This study found inelastic local buckling as the primary failure mode, with no global buckling. The flange and web width-thickness ratios, along with the axial force ratio, strongly influenced the hysteretic behaviour of H-shaped beam-columns. [9,33].

2.2. Development of FE models

This section introduces a validation study focused on refining modelling techniques for H-shaped carbon steel beam-columns with significant width-thickness ratios subjected to cyclic bending along the weak axis. In this study, SOLID185, which features eight nodes with three degrees of freedom at each node, was employed in ANSYS. Given that the material properties were not individually reported for each specimen, slight deviations from the numerical analysis may be anticipated compared to the relevant existing results. In FE models, mesh size significantly affects the results, with smaller meshes and more elements leading to longer solution times. To find the optimal element dimensions, a mesh sensitivity analysis was performed by reducing mesh size until differences between FE model outcomes and experimental data were minimal. Different mesh configurations, defined as very fine (2×2 mm^2), fine (5×5 mm^2), medium (10×10 mm^2), and coarse (30×30 mm^2), were tested. The fine mesh size (5×5 mm^2) was selected for its effectiveness in converging moment-rotation hysteresis curves, thereby ensuring accurate numerical responses. The mesh sensitivity analysis for the W-H1–0.2 sample, conducted to evaluate the influence of mesh size on the precision and computational efficiency of the FE model, is illustrated in Fig. 2.

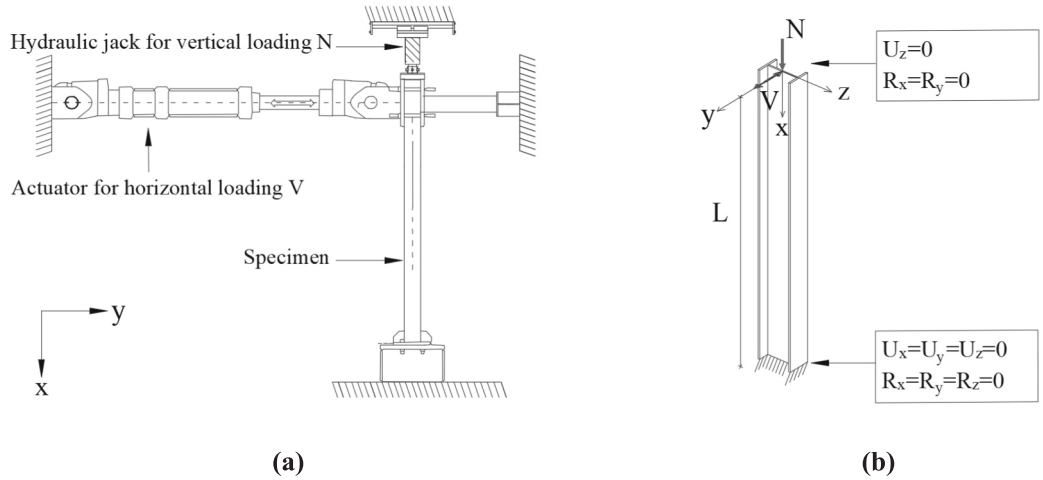

Fig. 1. Schematic diagram of setup and boundary condition: (a) Test setup, (b) Loading and boundary condition.

Table 1
Geometric parameters of the specimens from [33].

Specimen no.	$h \times b \times t_w \times t_f$	Nominal n
W-H1–0.2	300 × 200 × 6 × 4	0.2
W-H2–0.2	350 × 150 × 4 × 6	0.2
W-H3–0.3	350 × 175 × 4 × 4	0.2
W-H6–0.2	300 × 150 × 4 × 6	0.2
W-H6–0.4	300 × 150 × 4 × 6	0.4

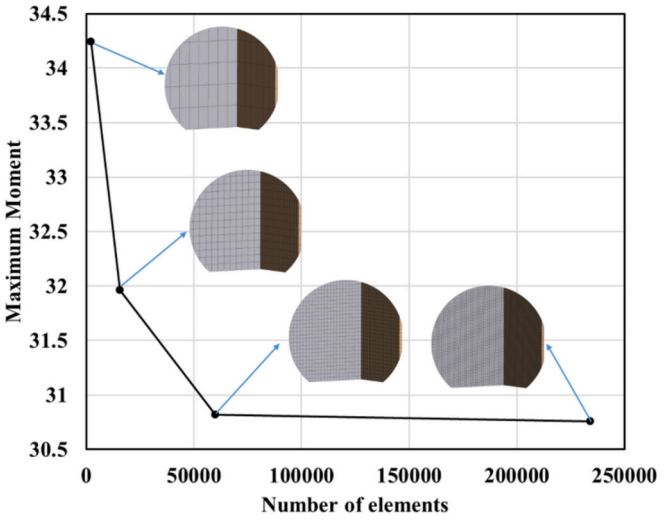

Fig. 2. Mesh convergence analysis for the W-H1–0.2 sample.

For the cross-section with welded joint, the contact with bonded formula were used. A multi-linear kinematic hardening law was employed according to [32]. The stress-strain responses were modelled in ANSYS in multi-linear form with 15 intervals. The material properties, measured and presented in Table 1 of [33], were used as the basis for this study. For the 4 mm plate, the actual thickness was 4.13 mm, with a yield stress of 479 MPa, an ultimate stress of 567 MPa, a modulus of elasticity of 2.01 × 10^5 MPa, and an elongation factor of 30.9 %. Similarly, the 6 mm plate had an actual thickness of 5.84 mm, a yield stress of 349 MPa, an ultimate stress of 530 MPa, a modulus of elasticity of 1.97 × 10^5 MPa, and an elongation factor of 37.3 %. These properties were used to derive the engineering stress-strain behaviour of the specimens according to [34]. This approach ensured consistency between the material properties and the numerical models used in the study. The true stress (σ_{true}) and logarithmic plastic strain (ε_{ln}^{pl}) were obtained from the engineering stress-strain responses according to Eqs. (1) and (2) respectively and integrated into the numerical models [35]. In the equations, σ_{nom} represents the engineering stress, ε_{nom} represents the engineering strain, and E is the Young's modulus.

$$\sigma_{true} = \sigma_{nom}(1 + \varepsilon_{nom}) \tag{1}$$

$$\varepsilon_{ln}^{pl} = ln(1 + \varepsilon_{nom}) - \sigma_{true}/E \tag{2}$$

The engineering stress-strain and true stress-strain responses for plates with thicknesses of 4 mm and 6 mm are illustrated in Fig. 3.

Geometric imperfections, which occur during transportation, fabrication, erection, and storage, can significantly affect the structural performance and resilience of elements. To account for these, imperfections corresponding to the lowest global and local buckling modes, identified through linear eigenvalue buckling analysis, were incorporated into the numerical models per [33]. The global imperfection amplitude was set at L/1000, [36] while the local imperfection amplitude followed the value proposed by Dawson and Walker [37], as shown in Eq. (3).

$$\omega_{D\&W} = 0.028\, t\left(f_y/\sigma_{cr}\right)^{1/2} \tag{3}$$

where, f_y is the yield stress and σ_{cr} is the critical elastic buckling stress of the slenderest constituent plate element of the section and t is the plate thickness. The test results indicate that local buckling governs the failure mechanism of all specimens, with no instances of global buckling observed. The first mode of local buckling of all specimens is shown in Fig. 4. While the local imperfection mode shape of W-H6–0.4 is not explicitly depicted in Fig. 4, it is identical to that of W-H6–0.2. This is due to the fact that both specimens share identical dimensional parameters, and the eigenvalue method was employed to extract the mode shapes. As a result, the local buckling mode without any external load remains consistent between the two specimens, making the representation of W-H6–0.2 applicable to W-H6–0.4.

The boundary conditions at the ends of the H-shaped columns were meticulously selected to replicate the experimental arrangement. The column base was fixed in all degrees of freedom to simulate the connection between the end plate and the laboratory floor. Moreover, the top faces were linked to a reference point located at the centroid of the column cross-section. As shown in Fig. 1, these top faces were restricted from lateral displacement along the Z axis and rotation in both the axial (ZY plane) and longitudinal (XZ plane) directions.

Geometric nonlinearity was activated to facilitate large displacement analysis by enabling the (*NLGEOM) option. Residual stresses were

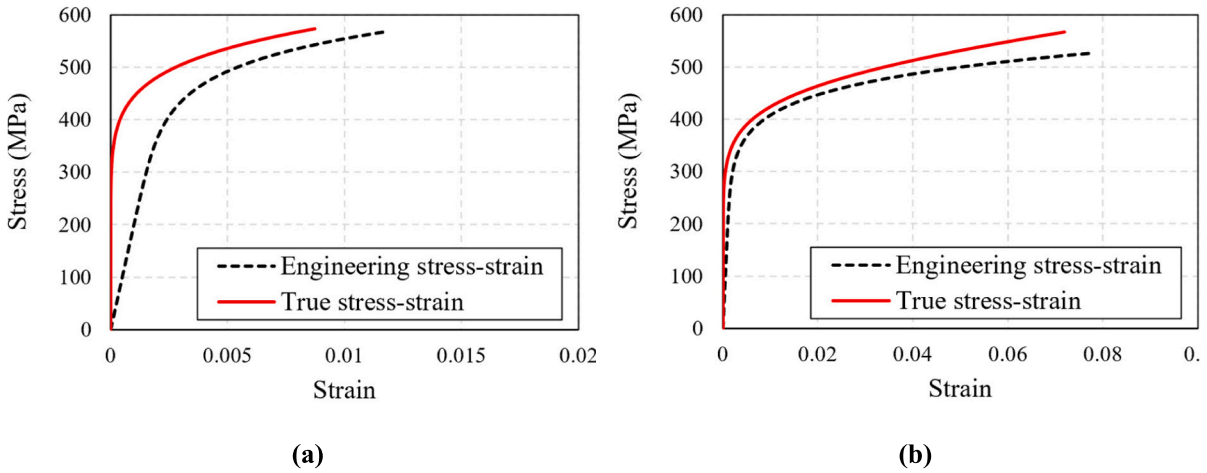

Fig. 3. Engineering and true stress-strain curves for (a) 4 mm thick plate and (b) 6 mm thick plate.

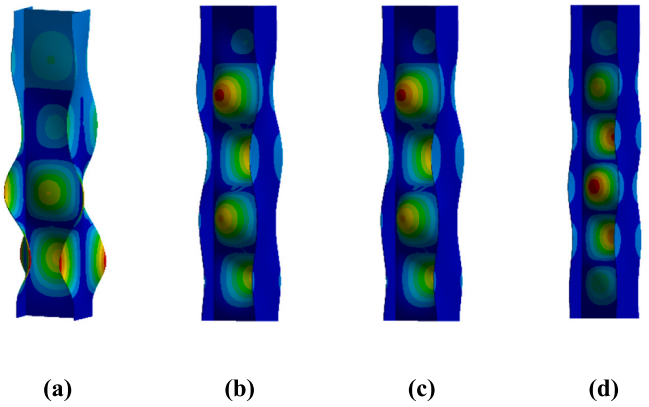

Fig. 4. Local imperfection mode shapes: (a) W-H1–0.2; (b) W-H2–0.2; (c) W-H3–0.2; (d) W-H6–0.2.

disregarded in this study since their effects were found to be negligible [38,39]. Initially, the axial load was applied to the FE models and subsequently maintained at a constant level. Illustrated in Fig. 5, a cyclic horizontal load was gradually increased, following the loading protocol presented in Fig. 4 of [33], and reached lateral displacement amplitudes of up to 10Δy.

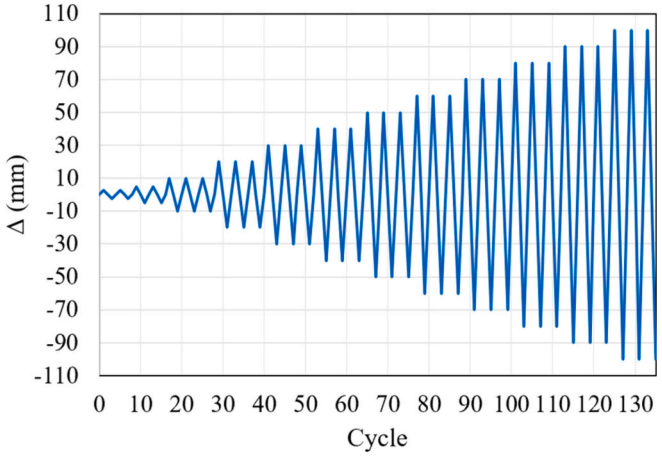

Fig. 5. Loading protocol [33].

2.3. Validation of the FE models

The validation study analysed five H-shaped carbon steel beam-column specimens with varying flange width-thickness ratios, web width-thickness ratios, and axial force ratios. Different steel plate configurations were used to investigate the interactive effects of these ratios on weak-axis hysteretic behaviour. The developed FE models were validated against experimental results, which entailed comparing various parameters such as the yield moment (M_{ec}), ultimate moment (M_u), moment-rotation hysteresis curves, M/M_{pc} -Rotation (θ) curve, and failure modes. As the number of results was extensive, only a few are presented here. The summary of the beam-column end moments and rotations from both the test and FE model is outlined in Table, with M_{ec}, M_u, and θ_y denoting the yield moment, ultimate moment, and yield rotation, respectively. Currently, no standardised method exists for determining yield rotation (θ_y); however, it is generally accepted that θ_y can be defined as the intersection point of a horizontal line at the ultimate moment (M_u) with the extension of the initial tangent stiffness line [40]. Furthermore, the yield rotation can be determined using elastic theory, where θ_y is expressed as M_{ec}/K_0, with K_0 representing the stiffness of the beam-column, given by $3EI/L$.

The developed models demonstrate a high level of predictive accuracy, as indicated in Table 2. On average, they predict the elastic and ultimate moment resistance, as well as yield rotation of the test specimens reported in the literature within a margin of 6.5 %. Additionally, Figs. 6 and 7 demonstrate that the predicted $M-\theta$ hysteretic curves and

Table 2
Comparison of the experimental and numerical results.

Parameter	Unit	Specimen no.				
		H-W1–0.2	H-W2–0.2	H-W3–0.2	H-W6–0.2	H-W6–0.4
M_{ec} (Test)	(kN.m)	22.6	12.3	17.4	12.3	9.2
M_{ec} (FE)	(kN.m)	21.93	11.78	18.24	11.52	8.96
K_0	(N/m)	2260	1352	1526	1353	1353
Error	%	2.96	4.24	4.84	6.36	2.61
M_u (Test)	(kN.m)	31.2	24.2	24.4	21.4	20.8
M_u (FE)	(kN.m)	30.82	25.02	23.69	22.48	22.38
Error	%	1.23	3.37	2.89	5.05	7.57
θ_y (Test)	(rad)	0.01	0.0091	0.0114	0.0091	0.0068
θ_y (FE)	(rad)	0.0097	0.0087	0.0119	0.0085	0.0066
Error	%	2.96	4.46	4.64	6.45	2.61

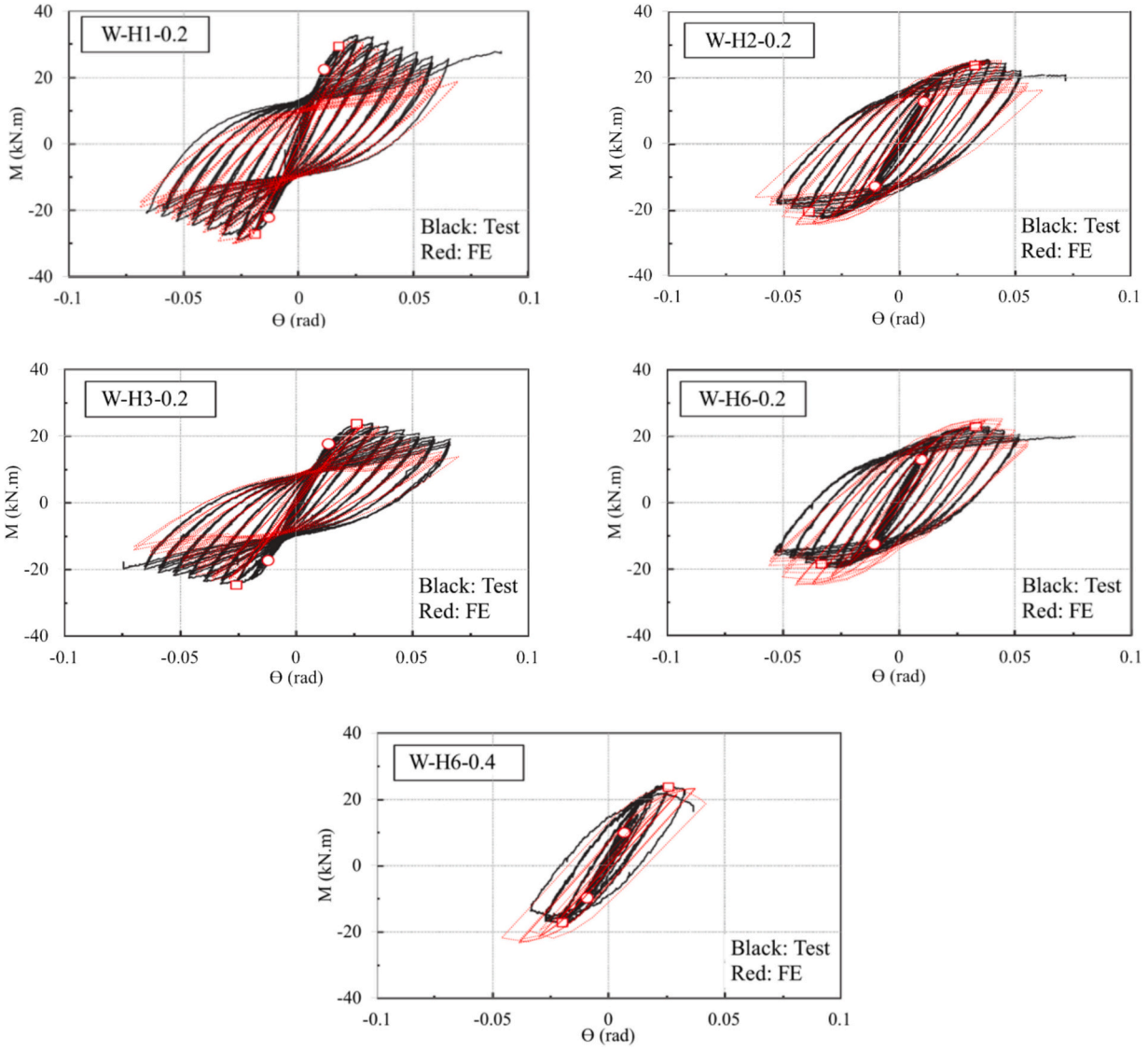

Fig. 6. Comparison of hysteresis curves: FE simulation vs. test results.

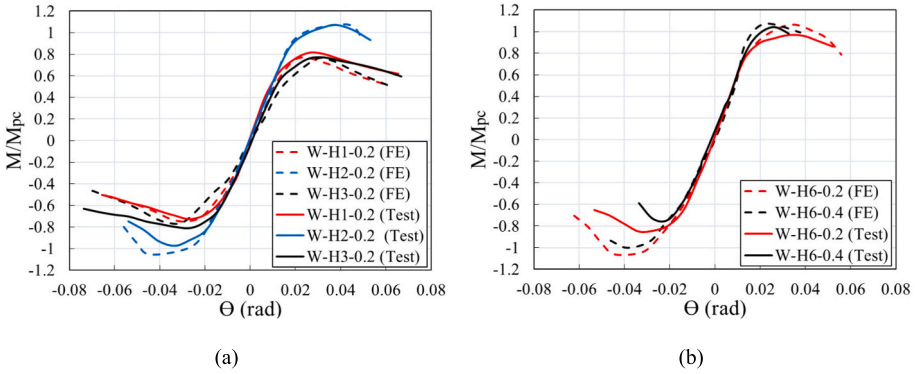

Fig. 7. Comparison of FE simulation and experimental M/M_{pc}-rotation: (a)W-H1, W-H2, W-H3 (b) W-H6.

the $M/M_{pc} - \theta$ curves exhibit a similar shape and pattern to the experimental curve. Nonetheless, the predicted stiffness of the hysteretic curve from FE models exceeds the measured stiffness for the specimens. Some inconsistencies between the test and FE results were noted in the M–θ and $M/M_{pc} - \theta$ diagrams, especially in the negative segment. References [16, 28, 38] suggest that the hysteresis diagram should show nearly symmetrical behaviour at critical points, such as yield moment, rotation, and ultimate moments. However, the observed asymmetry in the experimental hysteresis diagram led to discrepancies when validating the numerical results. This asymmetry is primarily attributed to

deformation of the supporting structure and possible slippage between the specimen's end plate and the support's upper surface. Therefore, in practical applications, the reinforced connection at the bottom may not function as an ideal rigid connection.

The failure modes observed in the FE models closely aligned with those in physical experiments, as shown in Fig. 8. Based on the comparisons between the FE models and the test results discussed in this section, it can be concluded that the FE models reliably produce accurate, consistent, and safe-side predictions of the test response. Therefore, they are suitable for conducting parametric studies on the cyclic performance of H-shaped steel beam-columns.

3. Parametric study

3.1. Design of experiments using Taguchi method

Genichi Taguchi developed statistical techniques, known as Taguchi methods, to improve the quality of manufactured goods. Recently, these methods have found applications in engineering as well [41–43]. The Taguchi method is a systematic and effective tool for system design, optimising parameter settings to minimise variation. In this section, this method is used to streamline multiple numerical analyses into a select few, ensuring accuracy.

The Taguchi method uses orthogonal arrays to optimise multiple variables with minimal experiments, outperforming traditional designs [42]. This study employed the Taguchi L27 orthogonal array with seven control factors, each at three levels: column length, stiffener spacing, material classification, section classification, load ratio, stiffener thickness, and number of local buckling modes. Table 3 outlines the control factors and levels. MINITAB software [44] generated the L27 array, covering all combinations of the seven factors across three levels, as shown in Table 4, which enables detailed analysis of factor interactions.

This study uses the Taguchi method's Main Effects Plot for Means to evaluate the impact of control factors on column ductility. By analysing mean responses, it identifies optimal ductility levels. Combining Taguchi design with ANOVA helps pinpoint significant variables and refine process parameters, enhancing the precision and effectiveness of optimisation. The Taguchi method was crucial in this study, significantly reducing the number of experiments. A factorial design would have required 2187 experiments, but the Taguchi method minimised effort while ensuring robust, reliable results.

Table 3
Control factors and levels.

Factor No.	Input parameters (Factors)	Levels		
		1	2	3
1	Length of column (mm)	1000	1500	2000
2	Stiffener spacing (mm)	250	500	750
3	Material	Austenitic	Ferritic	Duplex
4	Classification	Class 1	Class 3	Class 4
5	Load ratio	0.2	0.3	0.4
6	Stiffeners thickness (mm)	10	12	15
7	Local buckling modes No.	1	3	5

3.2. Finite element approach

After validating the FE models, a parametric study was conducted using the commercial software ANSYS [32]. Mesh operations followed the procedures outlined earlier. The eigenvalue buckling method identified global and local buckling modes, with the first global mode being bending. Initial load eccentricity was simulated by introducing a geometric imperfection of $L/1000$ at the column's mid-height. Column lengths (L) are listed in Table 4. Local imperfection amplitudes were incorporated into the FE models for stainless steel material using the Dawson and Walker model [45] according to Eq. (4), where $\sigma_{0.2}$ is the 0.2 % proof stress, t represents the plate thickness and σ_{cr} denotes the plate's critical elastic buckling stress. The Taguchi Design of Experiments control factor determines the number of the first local buckling mode, denoted as " local buckling modes No.".

$$\omega_0 = 0.023t\left(f_{0.2}/\sigma_{cr}\right) \tag{4}$$

The experiment used stiffeners of 10 mm, 12 mm, and 15 mm thickness, placed at distances of 250 mm, 500 mm, and 750 mm from the column's fixed bottom end. This arrangement, outlined in Table 4,

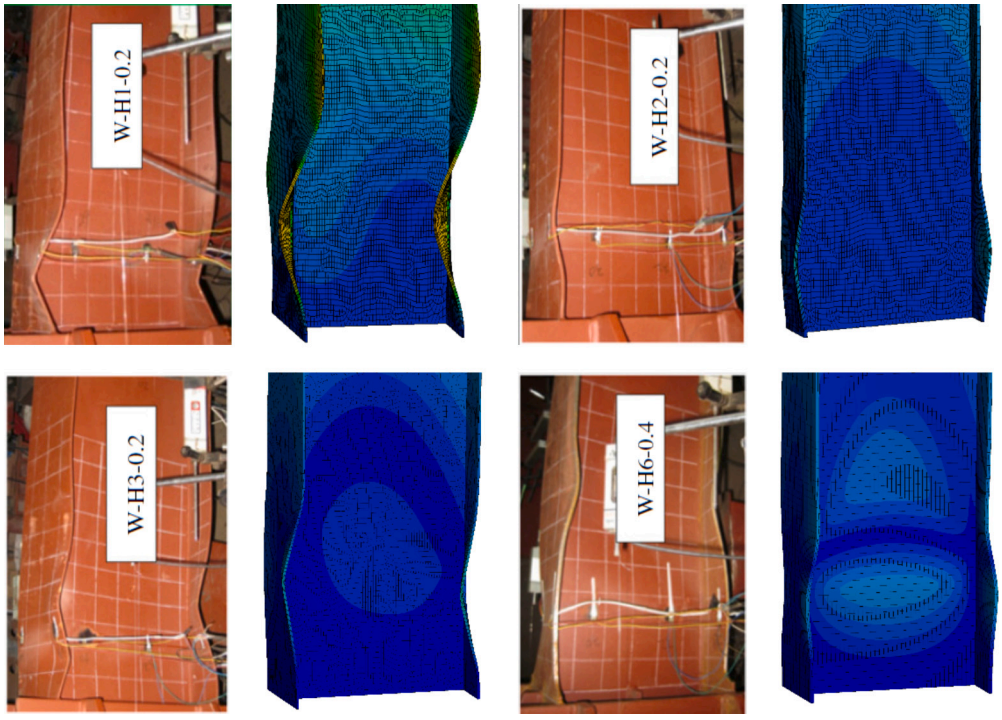

Fig. 8. Comparison of failure mode between FE result and test result (experimental work by [33]).

Table 4
TAGUCHI Design of Experiments L27 orthogonal array.

Case	Length (mm)	Stiffener spacing (mm)	Material	Classification	Load-ratio	Stiffener Thickness (mm)	Local buckling modes No.
1	1000	250	Austenitic	Class 1	0.2	10	1
2					0.3	12	3
3					0.4	15	5
4	1000	500	Ferritic	Class 3	0.2	10	1
5					0.3	12	3
6					0.4	15	5
7	1000	750	Duplex	Class 4	0.2	10	1
8					0.3	12	3
9					0.4	15	5
10	1500	250	Ferritic	Class 4	0.2	12	5
11					0.3	15	1
12					0.4	10	3
13	1500	500	Duplex	Class 1	0.2	12	5
14					0.3	15	1
15					0.4	10	3
16	1500	750	Austenitic	Class 3	0.2	12	5
17					0.3	15	1
18					0.4	10	3
19	2000	250	Duplex	Class 3	0.2	15	3
20					0.3	10	5
21					0.4	12	1
22	2000	500	Austenitic	Class 4	0.2	15	3
23					0.3	10	5
24					0.4	12	1
25	2000	750	Ferritic	Class 1	0.2	15	3
26					0.3	10	5
27					0.4	12	1

followed the Taguchi experimental setup to ensure consistency across all parametric study cases.

The parametric study used common carbon steel defined in Section 2 and key stainless steel grades: austenitic (EN 1.4571), ferritic (EN 1.4003), and duplex (EN 1.4462). Austenitic stainless steels with 17–18 % chromium and 8–11 % nickel offer excellent ductility, toughness, and corrosion resistance. Ferritic stainless steel is stronger than carbon steel but less ductile than Austenitic. Duplex stainless steel combines austenite and ferrite, providing greater strength but reduced deformability compared to austenitic grades. [28,46]. The modelling procedures from Section 2 were applied using the hot-rolled stainless steel properties from Afshan et al. [19], as detailed in Table 5, for the parametric numerical studies. This ensured an accurate representation of stainless steel's characteristics, including key mechanical properties [47], cross-sectional dimensions, and section classifications. Additionally, a multi-linear kinematic hardening model was employed in ANSYS where appropriate to capture the material's nonlinear behaviour.

Table 5 defines the following symbols: E represents Young's modulus, f_y is the yield stress (0.2 % proof stress), f_u is the ultimate tensile stress, and ε_u is the strain at ultimate tensile stress. The parameters n and m relate to the Ramberg-Osgood formulation [47], used to model the nonlinear stress-strain response of stainless steel. This material model, often used in a two-stage form, is described by Eqs. (5) and (6).

$$\varepsilon_\theta = (\sigma_\theta/E_\theta) + 0.002\left(\sigma \Big/ f_{y,\theta}\right)^{n_\theta}, \sigma \le f_{y,\theta} \tag{5}$$

$$\varepsilon_\theta = \frac{\sigma_\theta - f_{y,\theta}}{E_{0.2,\theta}} + \varepsilon_{u,\theta}\left(\frac{\sigma_\theta - f_{y,\theta}}{f_{u,\theta} - f_{y,\theta}}\right)^{m_\theta} + \varepsilon_{y,\theta}, f_{y,\theta} < \sigma \le f_{u,\theta} \tag{6}$$

The cross-sections used were H sections, with four numbers indicating section depth, width, web thickness, and flange thickness. Section classification calculations followed EN 1993-1-4 [48], categorising the cross-sections as shown in Table 5. This classification ensures compliance with design codes while accurately assessing local buckling resistance and determining slenderness limits. The impact of axial force ratio was analysed at three levels ($n = N/N_y$): 0.2, 0.3, and 0.4, where N_y is the nominal yield axial load.

Fig. 9 presents the true stress-strain curves used as input for the finite element (FE) models for all stainless steel materials, with the corresponding material properties detailed in Table 5.

4. Results and discussions

4.1. Hysteresis diagrams and ductility

This research examines the effects of seven parameters (Table 3) on the ductility of steel columns subjected to axial and cyclic lateral loads, utilising ANSYS. This is critical for seismic design, as ductility reflects the members' plastic deformability. The analysis focuses on the ductility ratio ($\mu = \theta_u/\theta_y$), where ultimate rotation (θ_u) corresponds to the rotation at ultimate moment strength.

Table 5
Material properties [47] and section classification [48].

Stainless steel grade	E (N/mm^2)	f_y (N/mm^2)	f_u (N/mm^2)	ε_u	n	m	Cross-section	Classification
Austenitic; EN 1.4571	200,000	280	580	0.5	9.1	2.3	H- 300 × 150 × 6 × 10	Class 1
							H- 300 × 150 × 4 × 6	Class 3
							H- 300 × 200 × 4 × 6	Class 4
Ferritic; EN 1.4003	200,000	320	480	0.16	17.2	2.8	H- 300 × 150 × 6 × 10	Class 1
							H- 300 × 200 × 6 × 10	Class 3
							H- 300 × 150 × 4 × 6	Class 4
Duplex; EN 1.4662	200,000	530	770	0.3	9.3	3.6	H- 300 × 100 × 6 × 10	Class 1
							H- 300 × 150 × 6 × 10	Class 3
							H- 300 × 200 × 6 × 10	Class 4

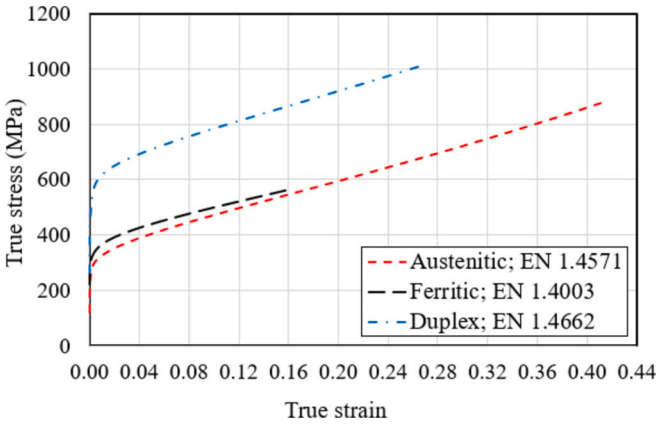

Fig. 9. True stress-strain curves for FE input of stainless steel materials.

By varying parameters within the design of experiments, the study examined their impact on structural performance under seismic conditions The hysteresis diagram results shown in Fig. 10 are compiled in Table 6, displaying the ductility ratios of the specimens.

After the FE analysis, Taguchi analysis was performed using Minitab v.22 to identify optimal conditions for each control factor and assess their impact on column ductility. Mean responses for each control factor level were calculated and organised in Table 7, showing the average effect of each factor. The results were plotted in Fig. 11 to illustrate the impact on ductility. (See Table 8.)

In Table 7, the mean responses represent average values for each factor and level. Delta shows the impact range by indicating the difference between the maximum and minimum mean responses for each factor. Factors are ranked by Delta, with column length ranked 1, indicating the most significant effect. The results in Table 7 and Fig. 11 show that length, stiffener spacing, material grade, and classification are the most influential factors, while imperfection, stiffener thickness, and load ratio have minimal impact.

Column length, with a Delta value of 4.833, significantly affects cyclic performance by influencing slenderness, buckling, stress distribution, and bending. Longer columns are more prone to buckling, lateral displacement, and flexural stress, reducing ductility and cyclic performance. Material nonlinearity and P-Delta effects further destabilise longer columns. Stiffener spacing ranks second, improving ductility by preventing local buckling and maintaining stability [49,50]. Though less impactful than column length and material grades, it helps manage buckling modes and delays plastic hinge formation, enhancing resilience. Column length affects buckling through slenderness, while material grades influence mechanical properties and energy dissipation, vital for overall stability. Material grade ranks third, with a mean

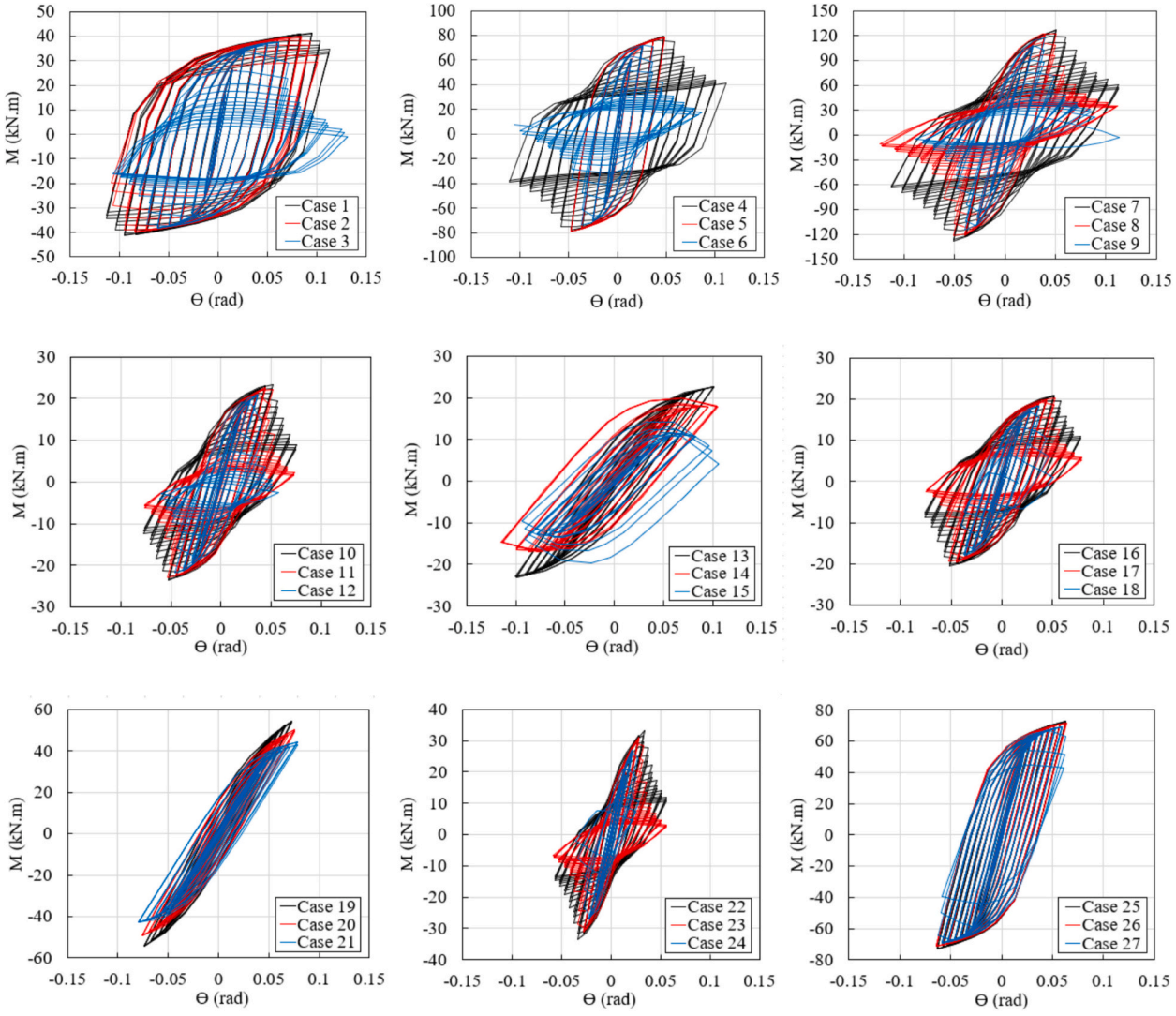

Fig. 10. Hysteresis diagram.

Table 6
Results for numerical analyses.

Case No.	M_{ec} (kN.m)	K_0 (N/m)	θ_y (rad)	M_u (kN.m)	θ_u (rad)	$\mu = \theta_u/\theta_y$
1	20.926	3378	0.0062	41.407	0.0949	15.31
2	20.298	3378	0.0060	40.106	0.0841	14.02
3	10.739	3378	0.0032	37.756	0.0611	19.09 (max)
4	49.512	8004	0.0062	79.308	0.0479	7.73
5	48.171	8004	0.0060	78.458	0.0483	8.05
6	46.746	8004	0.0058	72.429	0.0265	4.57
7	90.575	8004	0.0113	127.46	0.0507	4.49
8	88.396	8004	0.0110	122.04	0.0506	4.60
9	50.087	8004	0.0063	117.64	0.0397	6.30
10	16.394	1352	0.0121	23.328	0.0517	4.27
11	16.571	1352	0.0123	22.546	0.0447	3.63
12	12.025	1352	0.0089	20.971	0.037	4.16
13	13.92	668	0.0208	22.707	0.100	4.81
14	9.63	668	0.0144	19.968	0.069	4.79
15	5.57	668	0.0083	14.21	0.032	3.86
16	11.30	1352	0.0083	20.91	0.0518	6.24
17	10.70	1352	0.0079	20.31	0.0526	6.66
18	10.20	1352	0.0075	18.44	0.0369	4.92
19	26.80	1689	0.0159	54.56	0.0733	4.61
20	25.20	1689	0.0149	50.07	0.0758	5.09
21	13.30	1689	0.0079	44.21	0.0782	9.90
22	15.70	2400	0.0065	33.18	0.0339	5.22
23	15.30	2400	0.0064	31.04	0.0279	4.36
24	14.60	2400	0.0061	27.27	0.0217	3.56
25	40.20	1689	0.0238	72.76	0.0632	2.66
26	39.20	1689	0.0232	71.67	0.0637	2.75
27	38.80	1689	0.0229	69.14	0.059	2.58 (min)

response of 8.822. Stainless steel grades like austenitic, duplex, and ferritic significantly affect column performance under seismic loads due to their mechanical properties. Austenitic steel offers high deformation capacity, ideal for absorbing seismic energy, while duplex balances strength and deformability. Ferritic steel has lower deformability and is more prone to brittle failure. Material grade and stiffener spacing are nearly equal in influence, with only a 0.2 % difference in their delta values. As illustrated in Fig. 11, Class 1 sections have high ductility, allowing significant plastic deformation and excellent cyclic performance. Class 3 sections, limited by local buckling before reaching full plastic moment, show moderate ductility and reduced stability. Class 4 sections, buckling below the yield point, exhibit minimal ductility and poor cyclic response with rapid strength and stiffness loss. The number of local buckling modes has little effect on column ductility and cyclic performance, as local buckling mostly impacts slender section stability. Imperfections cause small geometric deviations that can accelerate local buckling during cyclic loading. However, global buckling and overall structural stability have a greater impact on performance. While imperfections slightly reduce ductility, they do not significantly affect energy dissipation or dominate the cyclic behaviour. Investigating stiffener thickness in H-section steel columns shows that minor changes do not significantly impact performance. Increasing the thickness from 10 mm to 12 mm improves ductility by enhancing stress distribution and preventing local buckling, allowing the structure to handle higher cyclic loads. However, at 15 mm, ductility decreases slightly due to reduced flexibility. Thicker stiffeners increase stiffness, limiting inelastic deformation and creating higher stress concentrations. This makes the structure more rigid, reducing its energy absorption and deformation capacity under cyclic loading. The balance between flexibility and stiffness shifts, hindering the structure's ability to dissipate energy and deform plastically. Optimal stiffness-flexibility balance is key to maximising cyclic performance. For the load ratio also, we observe structure's ability to absorb more energy during hysteretic cycles at load ratio of 0.4. The reason behind this is that higher load ratios induce larger plastic deformations, contributing to greater energy dissipation. However, the performance at lower load ratios shows an improved ductility, as these ratios don't reach the threshold for significant plastic deformation. Therefore, the load ratio's influence is tied not only to ductility but also to the overall energy dissipation capacity of the structure, which is critical during cyclic loading.

According to Fig. 11, the Standard Error of the Regression (S) is 1.806, indicating how closely observed values align with the regression line. The R-Squared (*R-Sq*) is 0.906, showing strong variability explanation by the independent variables, while the Adjusted R-Squared (*R-*

Table 8
Modal summary.

S	*R-Sq*	*R-Sq (adj)*
1.806	90.68 %	79.80 %

Table 7
The mean response for each level of every control factor.

Level	Length (mm)	Stiffener spacing (mm)	Material grade	Classification	Local buckling mode No.	Stiffener Thickness (mm)	Load ratio
1	9.360	8.917	8.822	7.777	6.520	5.857	6.142
2	4.812	5.213	4.483	6.412	5.778	6.440	5.988
3	4.527	4.569	5.393	4.510	6.401	6.402	6.569
Delta	4.833	4.348	4.339	3.267	0.742	0.583	0.581
Rank	1	2	3	4	5	6	7

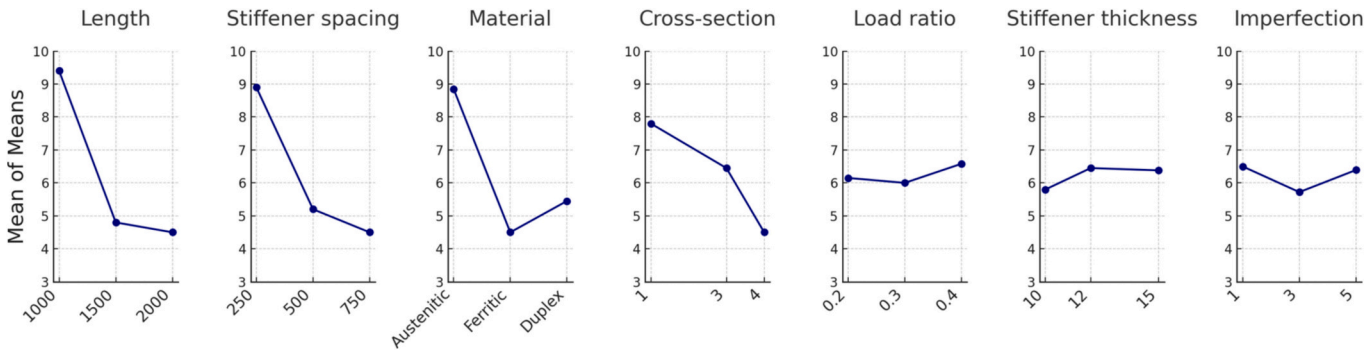

Fig. 11. Effect of levels of control factors on ductility (Values for lengths, stiffener spacing, and thickness are in millimeters).

Sq(*adj*)) is 0.798, accounting for predictors. High *R-Sq* and *R-Sq*(*adj*) values indicate a strong model fit, though residual error suggests unaccounted factors. Overall, lower S indicates precision, and the *R-Sq* metrics confirm model effectiveness, though further exploration of unexplained factors is advised.

To identify significant control parameters affecting column ductility, analysis of variance (ANOVA) was conducted, as shown in Table 9. The ANOVA table attributes data variability to the different factors in the model.

Table 9 shows that the first four control factors impact column ductility by 31.54 %, 23.61 %, 22.45 %, and 11.54 %, respectively. Lower *P*-values (< 0.05) indicate statistical significance. Thus, column length, stiffener spacing, material grade, and cross-section were identified as significant control parameters.

In general, Fig. 10 shows that increasing the axial load ratio from 0.2 to 0.3 slightly decreases ductility, but increasing it further to 0.4 improves overall ductility. Table 6 reveals that the lowest ductility ratios are found in the last three cases with ferritic material and a column length of 2000 mm, with case 27 (load ratio 0.4) showing the lowest. Conversely, the highest ductility ratios are observed in the first three cases, which feature a column length of 1000 mm and Austenitic material grade. The third case, with a load ratio of 0.4 and high axial force, shows the greatest ductility, followed by the first case with a load ratio of 0.2. These findings indicate that real plastic capacity may not be fully captured by the ductility ratio alone, underscoring the importance of also evaluating energy dissipation capacity.

4.2. Energy dissipation capacity

Given that structures must absorb seismic energy during earthquakes, assessing columns' energy dissipation capacity is crucial. In this section, the hysteresis curves of 27 cases depicted in Fig. 10 are analysed to evaluate this capacity. The hysteresis curve is key in seismic analysis, showing energy dissipation, stiffness and strength degradation, and ductility [51], all critical for seismic resilience. The accumulated energy dissipation (AED) is quantified from the hysteresis curve, representing the total energy dissipated during all loading cycles, illustrated by the area within each hysteresis loop.

The plots in Fig. 12 show the relationship between AED and loading cycles for all 27 cases. Initially, the AED changes minimally, indicating the column remains in its elastic range. Around 15–20 cycles, the AED increases across all cases, marking the column's transition into the elastic-plastic phase. The analysis shows an inverse relationship between AED and load ratio, with AED values highest at a load ratio of 0.2, followed by 0.3, and lowest at 0.4. This trend is most evident in the first nine cases, though some combinations of load ratio, local buckling modes, and stiffener thickness show slight deviations. While case 3 (load ratio 0.4) has the highest ductility, case 7 (load ratio 0.2) has the highest AED. Given the multiple factors affecting cyclic performance, including section size, classification, material grades, and load ratios, both AED and ductility must be considered to fully understand structural behaviour.

4.3. Effect of load ratio

To explore load ratio effects, Fig. 13 shows failure modes for three cases with the same material and length but load ratios of 0.2, 0.3, and 0.4. Despite slight changes in stiffener thickness, key differences emerge in the column's bottom sections. Case 1 (load ratio 0.2) shows a maximum strain of 0.083, Case 2 (ratio 0.3) reaches 0.178, and Case 3 (ratio 0.4) records 0.41, with plastic deformation more than doubling from 0.2 to 0.3 and increasing fivefold from 0.2 to 0.4. At lower load ratios, bending failure is predominant, with symmetric deformation at 0.2. However, increasing the load ratio to 0.3 disrupts this symmetry, resulting in uneven failure behaviour across the web, though the maximum deformation still occurs in the flanges. At a load ratio of 0.4, the deformation pattern resembles that at a load ratio of 0.3, but the maximum stress shifts to the web. As axial load levels increase, columns experience greater local buckling in the flanges and web, leading to more brittle and abrupt failures.

To highlight the differences in failure behaviour between stub and slender columns, Fig. 14 shows the failure mechanism and plastic strain propagation in 2000 mm columns for cases 19, 20, and 21. In these longer columns, the maximum plastic strain occurs on the flange farthest from the web. As the column length increases, higher load ratios amplify axial compressive forces, shifting the maximum strain toward the column's centre. The buckling pattern transitions from the first to higher modes, with plastic strain progressively spreading from the flanges to the web as the load ratio rises. This highlights the critical importance of considering both column length and load ratio when evaluating failure mechanisms in steel H-section columns.

4.4. Material comparison

To compare material performance, Case 10, with a 1500 mm column length, was analysed using austenitic, ferritic, and duplex stainless steels, along with carbon steel (CS). Axial force ratios of 0.2, 0.4, and 0.6 were used to assess the impact of load ratio across these materials. The hysteresis curves at a 0.2 load ratio, shown in Fig. 15(a), indicate that austenitic stainless steel has the highest ductility at 3.71, followed by ferritic and duplex steels at 3.69 and 3.02, respectively. Carbon steel exhibited the lowest ductility, at 2.1.

The moment-rotation hysteresis curves reveal that stainless steels, especially austenitic and duplex grades, outperform carbon steel under cyclic loading. Stainless steels show broader loops, indicating higher energy dissipation and better ductility, while carbon steel exhibits pinching and narrow loops, reflecting more stiffness loss and fatigue risk. Austenitic stainless steel shows strong cyclic stability with minimal degradation. Ferritic stainless steel behaves similarly but with narrower loops and more stiffness loss. Duplex stainless steel balances strength and ductility, whereas carbon steel experiences the greatest stiffness loss and fatigue susceptibility.

Carbon steel structures fail sooner and endure fewer loading cycles than stainless steel. Stainless steel's superior ductility allows for greater deformation and energy absorption, making it ideal for seismic applications. Its strain hardening, especially in austenitic and duplex grades,

Table 9
Analysis of Variance for Means.

Source	*DF*	*Seq SS*	*Adj SS*	*Adj MS*	*F*	*P*	Percent%
Length	2	132.377	132.377	66.1883	20.30	0.000	31.54
Stiffener spacing	2	99.098	99.098	49.5492	15.20	0.001	23.61
Material grade	2	94.234	94.234	47.1168	14.45	0.001	22.45
Classification	2	48.453	48.453	24.2264	7.43	0.008	11.54
Local buckling mode No.	2	2.861	2.861	1.4304	0.44	0.655	0.68
Stiffener thickness	2	1.918	1.918	0.9589	0.29	0.750	0.46
Load ratio	2	1.631	1.631	0.8154	0.25	0.783	0.39
Residual Error	12	39.128	39.128	3.2606			9.32
Total	26	419.699					100.00

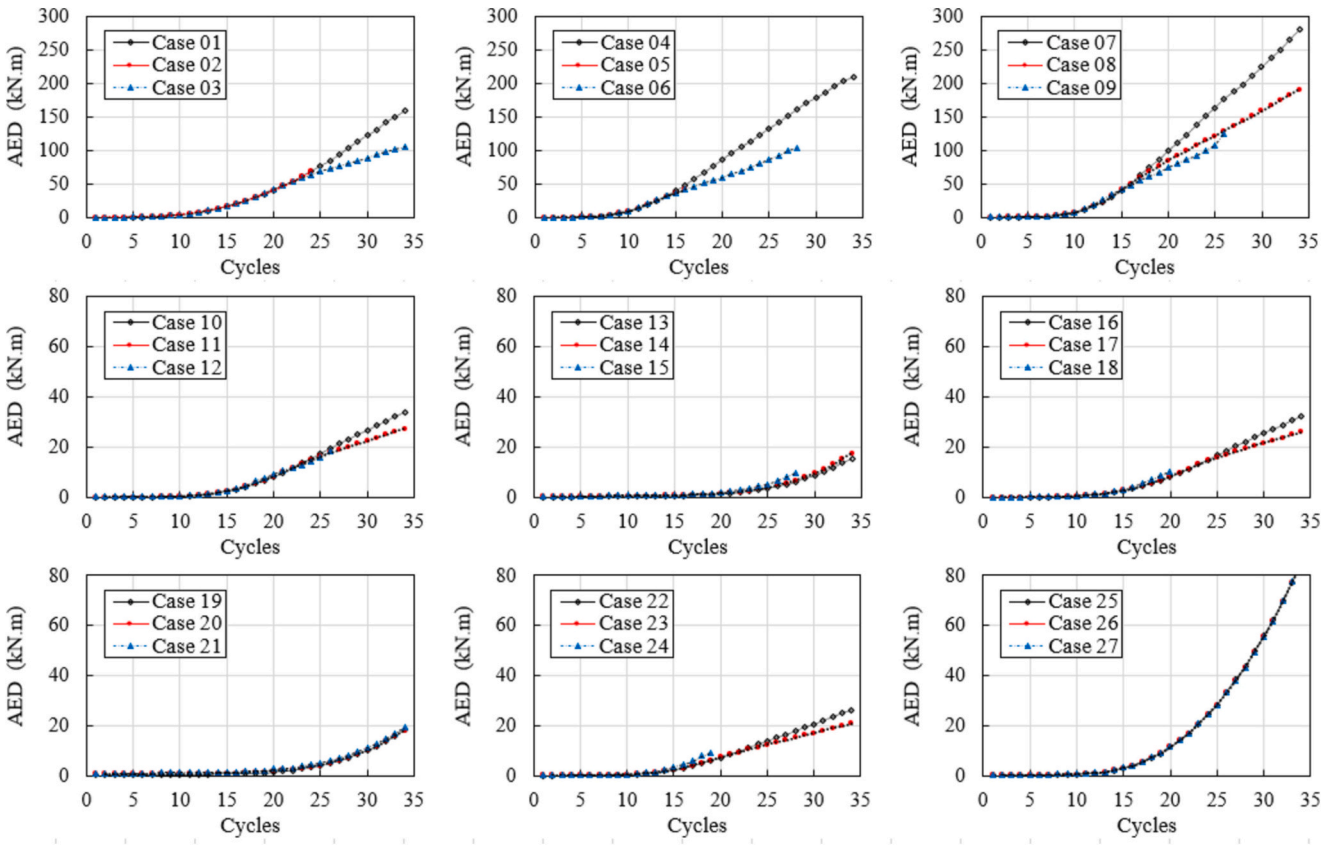

Fig. 12. Comparison of AED for all cases vs.loading cycles.

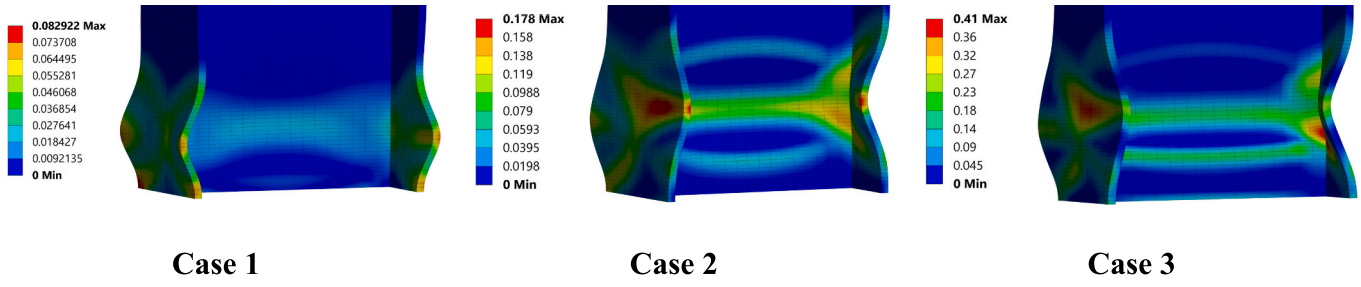

Fig. 13. Impact of Axial Load Ratios on plastic deformation and Failure Modes of Columns: Case Studies 1, 2, and 3.

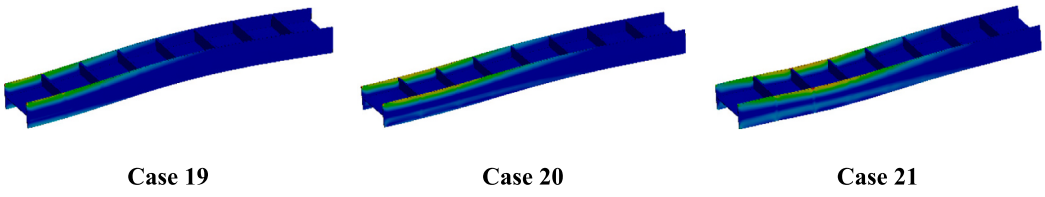

Fig. 14. Failure mechanism and plastic strain propagation- Case 19,20, and 21.

increases strength under repeated loads. With excellent corrosion resistance, stainless steel provides better long-term performance and durability. Examining the hysteresis curves at different load levels (0.2, 0.4, and 0.6) reveals distinct material performance differences. At 0.2, all materials show broader loops, indicating higher energy dissipation, with duplex and ferritic stainless steels absorbing more energy. Carbon steel, however, shows less hysteresis, indicating lower energy dissipation and stiffness degradation. At 0.4, pinching increases, especially for carbon steel, signalling significant stiffness loss. Stainless steels retain better cyclic stability. At 0.6, all materials experience pronounced pinching, with carbon steel showing the narrowest curve and reduced energy dissipation, while duplex stainless steel remains more resilient, though its performance also declines.

Fig. 16 shows the hysteretic load-displacement curves for various stainless steel grades and carbon steel under cyclic loading. The skeleton curves, connecting peak load-displacement points, depict the overall cyclic response. Austenitic and ferritic stainless steels exhibit relatively symmetric cyclic behaviour with smooth transitions between positive

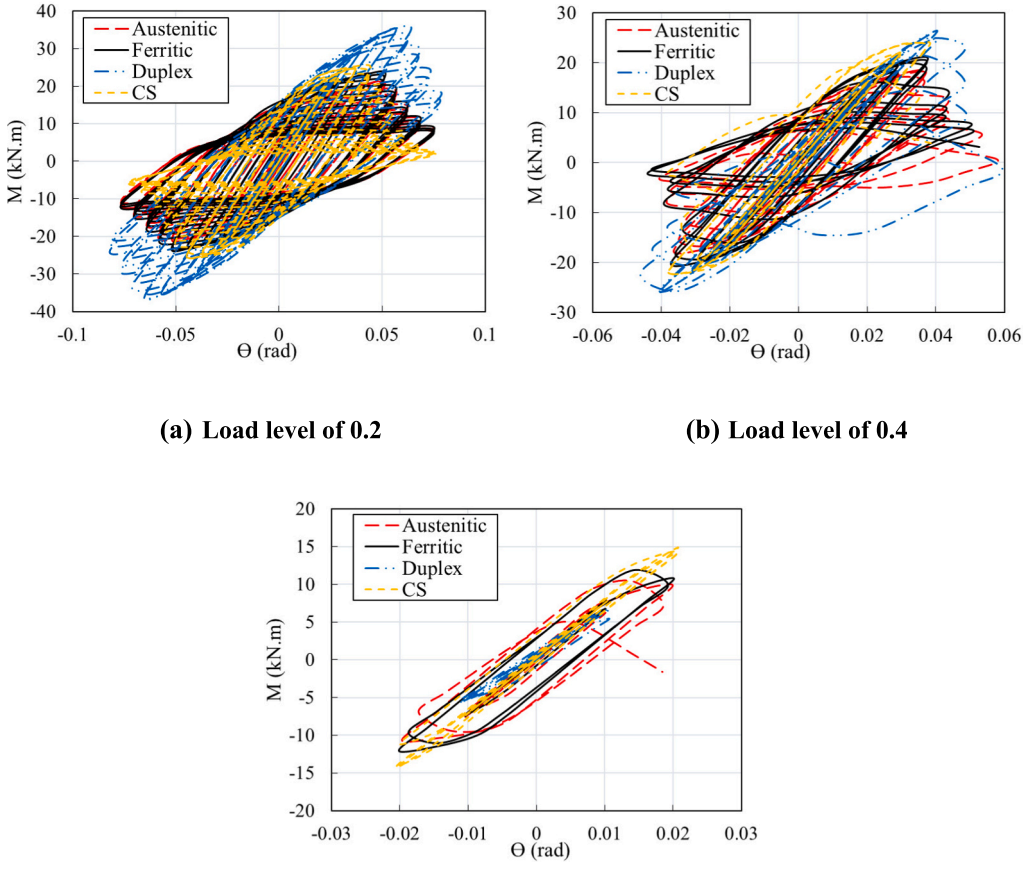

Fig. 15. Moment-rotation hysteresis curves for all materials for case 10, comparing load levels of 0.2, 0.4, and 0.6.

and negative loads, indicating consistent performance. In contrast, duplex steel shows a sharper response, suggesting increased stiffness.

In Fig. 16, austenitic steel (red) shows a ductile response with wider hysteresis loops, indicating higher energy dissipation. Ferritic (green) and carbon steel (yellow) exhibit pinched loops, reflecting reduced energy dissipation and potential degradation. Duplex steel (blue) has higher peak load capacity but narrower loops, suggesting less energy absorption than austenitic steel.

The skeleton curves provide critical insights into the failure modes of these materials, as shown in Fig. 17. reveal failure modes for different steels under cyclic loading, with maximum strain values shown. Austenitic stainless steel (0.122 max strain) has relatively uniform strain distribution, indicating moderate deformation without excessive localised failure. Ferritic stainless steel (0.143 max strain) shows more strain concentration near the flanges, suggesting a higher tendency for deformation but still stable behaviour. Duplex stainless steel (0.149 max strain) exhibits more localised strain, indicating higher stiffness and increased susceptibility to localised failure. Carbon steel (0.652 max strain) displays significant strain concentration, especially near the cross-sectional area, reflecting substantial localised deformation and a higher likelihood of failure.

In Fig. 18(a), the AED vs. cycles graph shows that duplex and austenitic stainless steels dissipate significantly more energy as cycles increase compared to carbon steel, which has the lowest AED. Ferritic stainless steel performs better than carbon steel but lags behind duplex and austenitic steels. As cycles increase, the gap widens, with duplex stainless steel showing the steepest AED rise, indicating superior energy absorption capacity under repeated loading.

In Fig. 18(b), duplex stainless steel shows the highest stress amplitude across cycles, followed by ferritic and austenitic steels, with carbon steel consistently lowest. Carbon steel stabilises after a modest initial increase, indicating limited strain hardening. In contrast, stainless steels, especially duplex, continue increasing in stress amplitude, showing superior strain hardening and cyclic performance. Ferritic and austenitic steels also rise but with lower amplitudes than duplex. As cycles increase, the gap widens, highlighting carbon steel's lower resilience compared to stainless steels.

A key limitation of this study is its use of simplified cyclic loading protocols, which don't fully reflect the complexity of real seismic events. Future research should explore more realistic multi-directional forces and include temperature variations, particularly under fire exposure, as these can affect steel's performance. Additionally, studying long-term fatigue under repeated, low-intensity tremors could improve design codes for regions with frequent seismic activity. Finally, while duplex and austenitic stainless steels perform well, their high costs limit use, so future work should focus on cost-effective solutions and life-cycle assessments to increase their viability.

5. Conclusion

This study investigates the seismic performance of steel columns using the Taguchi method for experimental design and the Finite Element Method (FEM) for simulations. Seven key parameters—column length, stiffener spacing, material classification, load ratio, stiffener thickness, and local buckling modes—were analysed. The Taguchi method, using an L27 orthogonal array, reduced the necessary tests from 2187 to 27 while ensuring reliable results. ANOVA identified column length, stiffener spacing, and material grade as the most critical factors

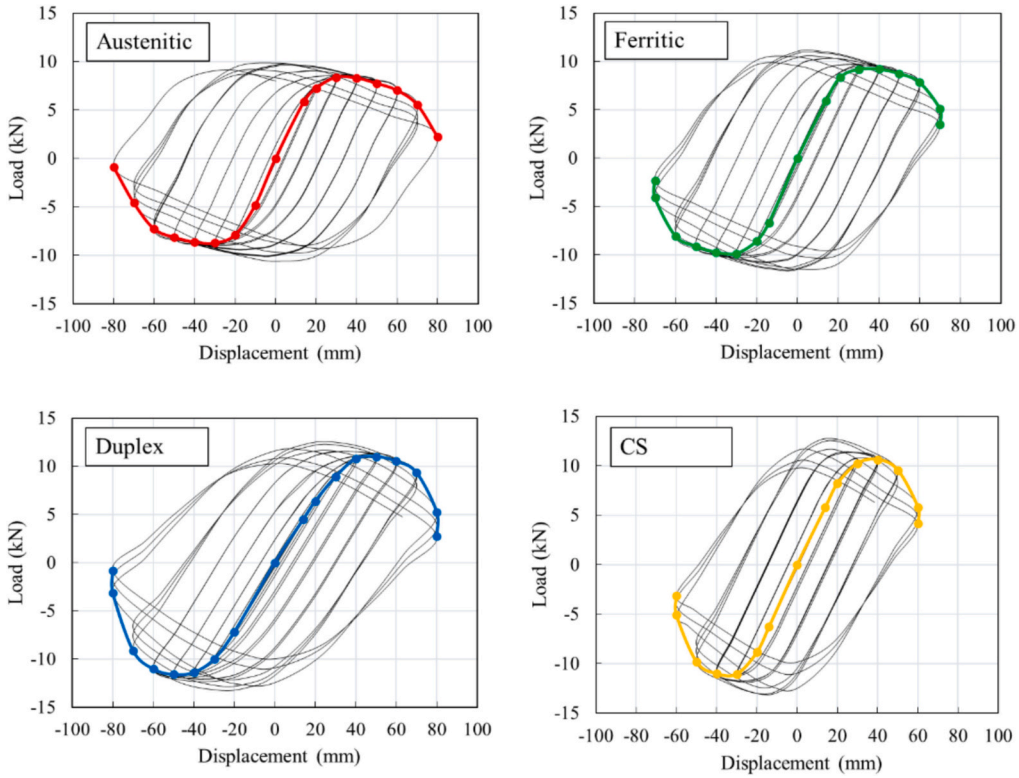

Fig. 16. Load-displacement hysteresis curves for all materials for case 10 with load level of 0.2.

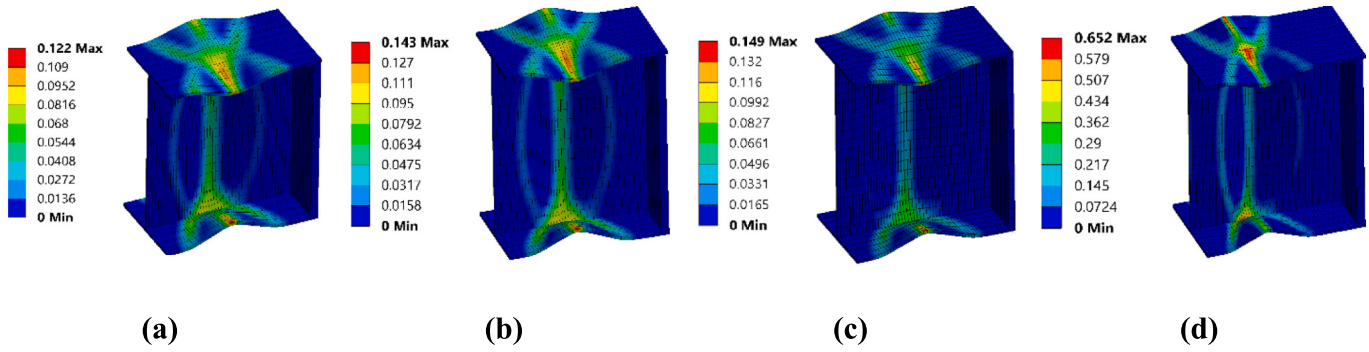

Fig. 17. Comparative Failure Mechanisms of Different Materials: a) Austenitic Stainless Steel, b) Ferritic Stainless Steel, c) Duplex Stainless Steel, d) Carbon steel.

affecting ductility under cyclic loading.

- Ductility ratios ranged from 19.09 for austenitic steel columns with a 0.4 load ratio to 2.58 for ferritic steel columns of 2000 mm at the same ratio.
- Longer columns showed reduced ductility due to increased slenderness and a higher risk of buckling.
- Stiffener spacing also played a key role, with closer spacing preventing local buckling and enhancing load-carrying capacity.
- Austenitic stainless steel showed the highest accumulated energy dissipation (AED), especially at a 0.2 load ratio, with broader hysteresis loops indicating better energy absorption and lower stiffness degradation.
- Duplex stainless steel exhibited narrower loops but higher maximum cyclic strength, indicating better stiffness retention. Its higher cyclic strength makes duplex steel ideal for seismic applications requiring strength under repeated loading.
- Austenitic stainless steel displayed the highest ultimate rotation capacity, meaning it can undergo large plastic deformations before failure, crucial for absorbing energy during earthquakes.
- Duplex stainless steel, with its higher cyclic strength, is beneficial for structures in seismic regions where resilience against intense loads is needed, though its narrower loops suggest lower energy absorption.

The analysis of failure modes revealed distinct behaviours among the materials.

- Austenitic stainless steel exhibited uniform strain distribution with a maximum strain of 0.122, indicating moderate deformation and strong resilience under cyclic loading.
- Ferritic stainless steel showed localised strain near the flanges, with a maximum strain of 0.143, reflecting a higher tendency for deformation but stable performance.
- Duplex stainless steel, with a maximum strain of 0.149, demonstrated increased stiffness and more concentrated strain, raising susceptibility to localised failures.

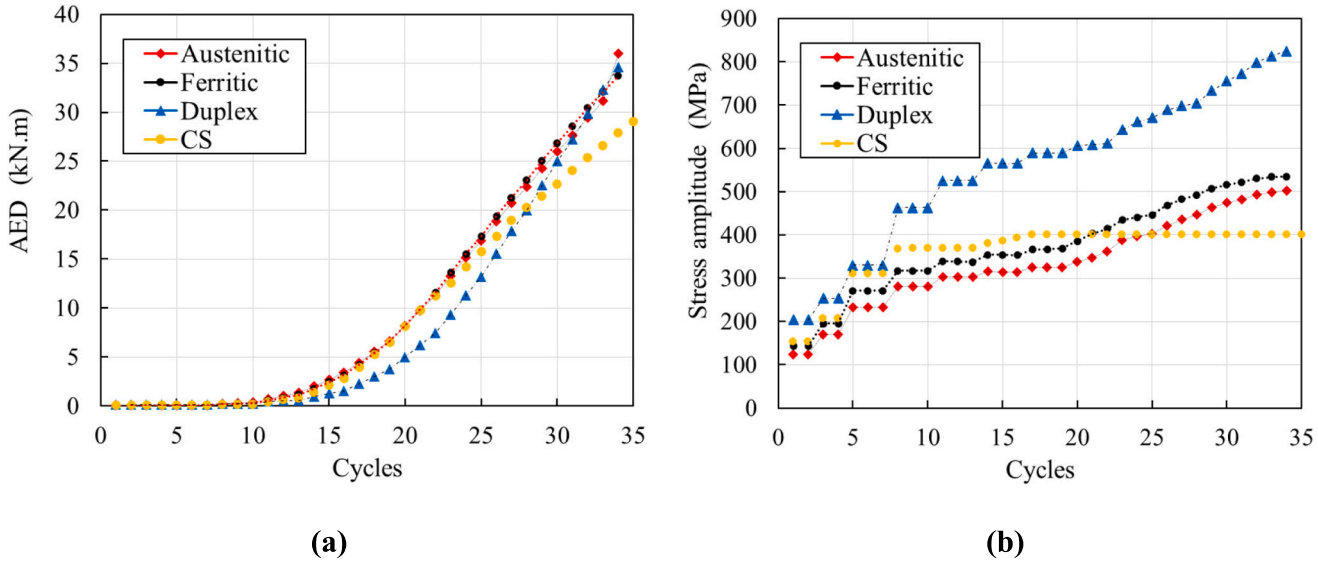

Fig. 18. Comparison of a) AED vs. cycles and b) stress amplitude (MPa) vs. cycles for carbon steel and different grades of stainless steel in case 10 column.

- Carbon steel experienced the most significant strain concentration (0.652), indicating a higher likelihood of brittle failure under seismic loads.

In conclusion, the study emphasizes optimising column length, stiffener spacing, and material selection for seismic applications. Austenitic stainless steel is ideal for seismic zones due to its high ductility and energy absorption, while duplex stainless steel offers strength and resilience where moderate ductility is sufficient. Ferritic stainless steel performs better than carbon steel and is suitable for less demanding applications, though it lacks the ductility of austenitic grades. For practical design applications, when the column length is significant and slenderness becomes a concern, it is recommended to use closer stiffener spacing in conjunction with high-performance materials, such as austenitic or duplex grades. This approach helps prevent local buckling and enhances the overall seismic resilience of the structure, particularly in critical seismic zones. However, this study simplifies real seismic conditions by using basic cyclic loading protocols. Future research should explore multi-directional loading and temperature effects to fully capture real-world behaviour.

Formatting of funding sources

This research did not receive any specific grant from funding agencies in the public, commercial, or not-for-profit sectors.

CRediT authorship contribution statement

Asal Pournaghshband: Writing – original draft, Supervision, Methodology, Investigation, Formal analysis, Data curation, Conceptualization. **Roham Maher:** Writing – review & editing, Validation, Software.

Declaration of competing interest

During the preparation of this work, the authors used ChatGPT in order to improve the quality of writing, including assistance with proofreading and drafting the manuscript more effectively. After using this tool/service, the authors reviewed and edited the content as needed and take full responsibility for the content of the publication. The authors declare that they have no known competing financial interests or personal relationships that could have appeared to influence the work reported in this paper.

Acknowledgements

I would like to express my sincere gratitude to Dr. Farzad Piadeh for his valuable contributions in editing and revising this work. I would also like to extend my appreciation to Dr. Lu Yang and Dr. Keyang Ning for their feedback and support in refining the draft of this paper.

Data availability

No data was used for the research described in the article.

References

[1] BSI, BS EN 1993-1-1:2005. Design of Steel Structures, Part 1–1: General Rules and Rules for Buildings, BSI, London, 2005.
[2] EN 1993-1-2, Design of Steel Structures-Part 1–2: General Rules-Structural Fire Design, European Committee for Standardisation, London, 2007 Jan 29.
[3] EN 1993-1-1, Eurocode 3: Design of Steel Structures - Part 1–1: General Rules and Rules for Buildings, European Committee for Standardization (CEN), Brussels, 2005.
[4] A.H. Zubydan, Inelastic second-order analysis of steel frame elements flexed about minor axis, Eng. Struct. 33 (2011) 1240–1250.
[5] Y. Xu, Y. Chen, X. Cheng, Hysteretic Behaviour of Lightweight Steel Portal Frame: The 6th International Conference on Thin-Walled Structures, 2011.
[6] Y. Bu, L. Gardner, Finite element modelling and design of welded stainless steel I-section columns, J. Constr. Steel Res. 152 (2019) 57–67.
[7] Y.J. Shi, M. Wang, Y.Q. Wang, Experimental and constitutive model study of structural steel under cyclic loading, J. Constr. Steel Res. 67 (8) (2011) 1185–1197.
[8] Y.Y. Chen, X. Cheng, The concept of 'buckling hinge' in H-shaped steel member with non-plastic element and the usage in seismic design, in: IStructE Conference on Structural Engineering in Hazard Mitigation, 2013.
[9] X. Cheng, Y. Chen, L. Pan, Experimental study on steel beam–columns composed of slender H-sections under cyclic bending, J. Constr. Steel Res. 88 (2013) 279–288.
[10] Y.Y. Chen, X.X. Wu, H. Tian, J. Zhao, Y. Ma, Experiment on non-compact H-shaped members and frames subjected to cyclic loads and the prediction of capacities, Int. J. Steel Struct. 6 (3) (2006) 215–226.
[11] A.H. da Silva, A. Tsiavos, B. Stojadinovic, Ductility-strength and strength-ductility relations for a constant yield displacement seismic design procedure, Bull. Earthq. Eng. 21 (9) (2023) 4449–4479.
[12] X. Yang, H. Ban, Q. Yang, Y. Shi, L. Ma, Experimental and numerical studies on cyclic behaviour of superior high-performance steel welded I-section beam-column, J. Constr. Steel Res. 184 (2021) 106789.
[13] L. Gardner, The use of stainless steel in structures, Prog. Struct. Eng. Mater. 7 (2) (2005) 45–55.
[14] K.H. Nip, L. Gardner, A.Y. Elghazouli, Cyclic testing and numerical modelling of carbon steel and stainless steel tubular bracing members, Eng. Struct. 32 (2010) 424–441.
[15] L. Gardner, Stability and design of stainless steel structures: review and outlook, Thin-Walled Struct. 141 (2019) 208–216.
[16] Y. Chen, F. Zhou, R. Zhang, Y. Chi, Experimental study on seismic behaviour of welded H-section stainless steel beam-columns, Eng. Struct. 259 (2022) 114105.

[17] Y. Chen, F. Zhou, S. Zheng, J. Li, C. Shang, X. Lin, Influence of cyclic hardening characteristic on seismic performance of welded austenitic stainless steel H-section beam-column, Eng. Struct. 288 (2023) 116210.
[18] K.H. Nip, L. Gardner, C.M. Davies, A.Y. Elghazouli, Extremely low cycle fatigue tests on structural carbon steel and stainless steel, J. Constr. Steel Res. 66 (2010) 96–110.
[19] G. Kang, N. Ohno, A. Nebu, Constitutive modelling of strain range dependent cyclic hardening, Int. J. Plast. 19 (2003) 1801–1819.
[20] B. Hwang, T. Kim, Y. Kim, J. Kim, A comparative study on hysteretic characteristics of austenitic stainless steel and carbon steel slit dampers under cyclic loading, J. Build. Eng. 45 (2022) 103553.
[21] R.H. Kim, T.S. Kim, S.H. Im, Y. Xi, Hysteretic behaviour comparison of austenitic and lean duplex stainless steel square hollow section members under cyclic axial loading, Eng. Struct. 237 (2021) 112227.
[22] S. Zheng, F. Zhou, J. Cheng, H.T. Li, R. Rong, Experimental study on cyclic hardening characteristics of structural stainless steels, J. Constr. Steel Res. 191 (2022) 107196.
[23] L. Chen, X. Yao, Z. Sun, D. Wang, Study seismic performance of duplex stainless steel under large strain amplitude by cyclic loading test, J. Constr. Steel Res. 194 (2022) 107332.
[24] F. Zhou, L. Li, Experimental study on hysteretic behaviour of structural stainless steels under cyclic loading, J. Constr. Steel Res. 122 (2016) 94–109.
[25] I. Gonzalez-de-Leon, I. Arrayago, E. Real, E. Nastri, Rotation capacity of cold-formed stainless steel RHS beams under cyclic loading, J. Constr. Steel Res. 192 (2022) 107199.
[26] I. Gonzalez-de-Leon, E. Nastri, I. Arrayago, R. Montuori, V. Piluso, E. Real, Experimental programme on austenitic stainless steel RHS members subjected to monotonic and cyclic bending, Eng. Struct. 302 (2024) 117258.
[27] H. Moghaddam, A. Sadara, S.R. Jalali, Seismic performance of stainless-steel built-up box columns subjected to constant axial loads and cyclic lateral deformations, Structures 33 (2021) 4080–4095.
[28] K.Y. Ning, L. Yang, H.Y. Ban, Y.N. Sun, Experimental and numerical studies on hysteretic behaviour of stainless steel welded box-section columns, Thin-Walled Struct. 136 (2019) 280–291.
[29] K.Y. Ning, L. Yang, H.Y. Ban, Seismic performance of welded stainless steel H-section columns under cyclic horizontal loading, J. Struct. Eng. 147 (4) (2021) 04021016.
[30] F. Zhou, C. Fang, Y. Chen, Experimental and numerical studies on stainless steel tubular members under axial cyclic loading, Eng. Struct. 171 (2) (2018) 72–85.
[31] European Committee for Standardization (CEN), prEN 1998–1-2. Eurocode 8: Design of Structures for Earthquake Resistance – Part 1–2: Rules for New Buildings. Brussels, Belgium, 2023.
[32] ANSYS, ANSYS® Academic Research—Mechanical, Release 18.1, 2024.
[33] X. Cheng, Y. Chen, D.A. Nethercot, Experimental study on H-shaped steel beam-columns with large width-thickness ratios under cyclic bending about weak-axis, Eng. Struct. 49 (2013) 264–274.
[34] L. Gardner, Yun Xiang, Description of stress-strain curves for cold-formed steels, Constr. Build. Mater. 189 (2018) 527–538.
[35] W. Li, H.T. Fan, H. Ye, X.C. Lin, L.M. Chen, Finite element analysis and parametric study of panel zones in H-shaped steel beam–column joints, Buildings 13 (11) (2023) 2821.
[36] S. Afshan, O. Zhao, L. Gardner, Standardised material properties for numerical parametric studies of stainless steel structures and buckling curves for tubular columns, J. Constr. Steel Res. 152 (2019) 2–11.
[37] R.G. Dawson, A.C. Walker, Post-buckling of geometrically imperfect plates, J. Struct. Div. ASCE 98 (1) (1972) 75–94.
[38] S. Chen, X. Chen, Y.B. Wang, Z. Lu, G.Q. Li, Experimental and numerical investigations of Q690D H-section columns under lateral cyclic loading, J. Constr. Steel Res. 121 (2016) 268–281.
[39] L. Gardner, D.A. Nethercot, Numerical modeling of stainless steel structural components: A consistent approach, J. Struct. Eng. (2004) 1586–1601.
[40] C. Fang, F. Zhou, C. Luo, Cold-formed stainless steel RHSs/SHSs under combined compression and cyclic bending, J. Constr. Steel Res. 141 (2018) 9–22.
[41] J.L. Rosa, A. Robin, M.B. Silva, C.A. Baldan, M.P. Peres, Electrodeposition of copper on titanium wires: Taguchi experimental design approach, J. Mater. Process. Technol. 209 (2009) 1181–1188.
[42] İ. Türkmen, R. Gül, C. Çelik, A Taguchi approach for investigation of some physical properties of concrete produced from mineral admixtures, Build. Environ. 43 (6) (2008) 1127–1137.
[43] M. Nalbant, H. Gökkaya, G. Sur, Application of Taguchi method in the optimization of cutting parameters for surface roughness in turning, Mater. Des. 28 (2007) 1379–1385.
[44] L.L.C. Minitab, Getting Started with Minitab, Available from: www.minitab.com, 2024.
[45] M. Ashraf, L. Gardner, D.A. Nethercot, Finite element modelling of structural stainless steel cross-sections, Thin-Walled Struct. 44 (10) (2006) 1048–1062.
[46] K.A. Cashell, N.R. Baddoo, Ferritic stainless steels in structural applications, Thin-Walled Struct. 83 (2014) 169–181.
[47] L. Gardner, D.A. Nethercot, Experiments on stainless steel hollow sections-part 1: material and cross-sectional behaviour, J. Constr. Steel Res. 60 (9) (2004) 1291–1318.
[48] EN 1993-1-4, Eurocode 3: Design of Steel Structures – Part 1.4: General Rules Supplementary Rules for Stainless Steels, European Committee for Standardization (CEN), Brussels, 2015.
[49] A. Sventikov, D. Kuznetsov, Analysis of stiffening bar influence on rib local stability and stability of steel frame of double-tee variable by height cross-section, Struct. Mech. Struct. 1 (16) (2018) 75–85.
[50] Sventikov A, Kuznetsov D. Evaluation of the influence of the stiffeners on the overall stability of the variable-rigidity steel frame using FEM. Int Sci Conf Far East Con 2018: Mater Sci Constr 463:022091.
[51] Y. Zhong, Y. Liu, S. Liu, R. Feng, Seismic design of cold-formed steel beams based on flexural capacity-ductility-energy dissipation, Thin-Walled Struct. 192 (2023) 111171.